




NOVEMBER 11 2024

## Acoustic imaging of geometrically shielded sound sources using tailored Green's functions

Lican Wang ; Zhenjun Peng; Bao Chen; Zhida Ma; Wangqiao Chen; Peng Zhou ; Guocheng Zhou; Siyang Zhong 



*J. Acoust. Soc. Am.* 156, 3102–3111 (2024)

<https://doi.org/10.1121/10.0034353>



View  
Online



Export  
Citation

### Articles You May Be Interested In

Experimental study of airfoil-rotor interaction noise by wavelet beamforming

*J. Acoust. Soc. Am.* (May 2020)

Experimental investigation of the effect of sectional airfoil profile deviation on propeller noise

*Physics of Fluids* (February 2023)

Aeroacoustic investigation of side-by-side urban air mobility aircraft in full configuration with ground effect




*Physics of Fluids* (August 2024)



LEARN MORE

Advance your science and career as a member of the  
**Acoustical Society of America**

# Acoustic imaging of geometrically shielded sound sources using tailored Green's functions

Lican Wang,<sup>1</sup>  Zhenjun Peng,<sup>1</sup> Bao Chen,<sup>2</sup> Zhida Ma,<sup>1</sup> Wangqiao Chen,<sup>1,a)</sup> Peng Zhou,<sup>1</sup>  Guocheng Zhou,<sup>2</sup> and Siyang Zhong<sup>3,b)</sup> 

<sup>1</sup>Department of Mechanical and Aerospace Engineering, The Hong Kong University of Science and Technology, Clear Water Bay, Kowloon, Hong Kong Special Administrative Region of China

<sup>2</sup>AVIC-Aerodynamics Research Institute, Harbin, China

<sup>3</sup>Department of Aeronautical and Aviation Engineering, The Hong Kong Polytechnic University, Hung Hom, Hong Kong Special Administrative Region of China

## ABSTRACT:

In light of the growing market of urban air mobility, it is crucial to accurately detect the stationary or moving noise sources within the complex scattering environments caused by aircraft structures such as airframes and engines. This study combines conventional and wavelet-based beamforming techniques with an acoustic scattering prediction method to develop an acoustic imaging approach that considers scattering effects. Tailored Green's function is numerically evaluated and used to compute the steering vectors and the specific delayed time used in those beamforming methods. By examining common scenarios where a scatterer is positioned between the source plane and the array plane, it is observed that beamforming in a scattering environment differs from that in free space, leading to improved resolution alongside scattering-induced side lobes. The effectiveness of the developed method is validated through numerical simulations and experimental studies, confirming its improved ability to localize both stationary and rotating sound sources in a shielded environment. This advancement offers effective techniques for acoustic measurement and fault monitoring in the presence of structural scatterers. © 2024 Acoustical Society of America.

<https://doi.org/10.1121/10.0034353>

(Received 16 September 2024; revised 9 October 2024; accepted 13 October 2024; published online 11 November 2024)

[Editor: Didier Dagna]

Pages: 3102–3111

## I. INTRODUCTION

Acoustic imaging is important for localizing, quantifying, and characterizing noise sources, typically achieved through acoustic holography in near-field regions and beamforming techniques in far-field regions (Chiariotti *et al.*, 2019; Merino-Martínez *et al.*, 2019). Beamforming involves the utilization of sound pressure or velocity signals captured by a microphone array to conduct non-contact experiments (Chiariotti *et al.*, 2019), which has been widely utilized in industries such as aviation, aerospace, navigation, and rail transportation to offer valuable insights for noise control and reduction. The delay-and-sum beamforming technique is a classic time-domain approach in acoustic imaging. Variations in microphone positions within the array lead to sound waves emanating from a source reaching different microphones at different times. By delaying and summing these signals, the position of the sound source can be identified. To accelerate the calculation of specific-frequency cases and reduce errors in the translation of time-domain signals, the beamforming method is converted into the frequency domain through Fourier transformation. Since then, the frequency-domain technique has undergone significant enhancements over the decades, incorporating methodologies such as deconvolutional

(Brooks and Humphreys, 2006; Sijtsma, 2007), functional (Dougherty, 2014), adaptive (Huang *et al.*, 2012), and compressive sensing (Zhong *et al.*, 2013), as referenced in Chiariotti *et al.* (2019) and Merino-Martínez *et al.* (2019). The applicability of these methods in free-space propagation environments has been repeatedly demonstrated, whereas in the current stage, it is worth considering more practical and complicated configurations such as the effects of scattering bodies.

The steering vector in the beamforming process necessitates prior knowledge of sound propagation in the form of Green's function, while the presence of a scattering body may influence sound propagation through absorption and scattering (including reflection, diffraction, and shielding). The common scenario is the ground effect, a phenomenon frequently observed outside the optimal conditions of a non-reflective anechoic chamber. Representative examples include acoustic imaging of aircraft flyover noise, highway passing noise, and ship noise reflected by the sea surface. Typically, the ground effect can result in changes to sound pressure level, necessitating correction through a half-space Green's function rather than a free-field Green's function. Additional instances of scattering manifest in the enclosed rectangular section of a duct and a room, where multiple walls contribute to increased interference. This challenge has been addressed through the application of an image source method (Fischer and Doolan, 2017; Guidati *et al.*,

<sup>a)</sup>Email: wqchen@ust.hk

<sup>b)</sup>Email: siyang.zhong@polyu.edu.hk

2002), either with or without flow effects. Concerning other canonical geometries like airfoil (Amiet, 1975; Zhong *et al.*, 2020) and sphere (Mao *et al.*, 2015; Siozos-Rousoulis *et al.*, 2017), specific analytical solutions about the scattering effects are also available.

Beyond analytical approaches, experimental measurements can be applied to more general and realistic situations involving scattering (Bousabaa *et al.*, 2018; Fenech and Takeda, 2007). In these setups, the position of a reference sound source was adjusted to obtain a series of Green's functions from the sources to the microphones. For situations with airflow, a plasma-based source is particularly suitable for non-intrusive sound generation (Bahr *et al.*, 2015). Simultaneously, numerical methods such as large eddy simulations and linearized Euler equations were adopted to characterize sound propagation, which has been applied for both two- and three-dimensional beamforming (Bousabaa *et al.*, 2018; Lacombe *et al.*, 2013; Zhou *et al.*, 2024). To further improve the computational efficiency, geometric acoustics (Guo, 2024; Sarradj, 2017) and boundary methods (Hirayama *et al.*, 2022; Lehmann *et al.*, 2022; Lehmann *et al.*, 2024) were adopted for obtaining the tailored Green's function in the presence of scattering bodies. These tailored Green's functions have been thoroughly examined with stationary sources in the presence of scattering bodies. In this study, rotational sound sources that experience shielding are considered, where "shielding" refers to the absence of a direct path from the source to certain microphones (Henty and Stancil, 2004; Vieira *et al.*, 2019). Such a complex scenario is prevalent in the noise monitoring of modern urban air transportation systems such as the rotor noise scattered by the fuselage (Sagaga and Lee, 2024).

In this context, a scattering prediction method involving an equivalent source method and truncated singular value decomposition has been adopted to compute the tailored Green's function, through which the conventional frequency-domain beamforming method and the wavelet-based beamforming method are extended and applied for stationary and rotational sound source localization in a scattering environment, respectively. It is noted that the wavelet-based beamforming method employed in this study requires additional consideration of time delays induced by scattering, which distinguishes it fundamentally from previous frequency-domain methods (Hirayama *et al.*, 2022; Lehmann *et al.*, 2022). A benchmark scenario involving spherical scattering is utilized for numerical validation. Subsequently, acoustic experiments are conducted in an anechoic chamber to examine the proposed methodologies for shielded rotating sources.

The structure of this study is as follows. The methodologies of acoustic imaging with consideration of scattering are developed and implemented in Sec. II. The developed method is examined in Sec. III, with the conclusions drawn in Sec. IV.

## II. ACOUSTIC IMAGING METHOD

In this section, the method of conventional beamforming is first introduced to show some fundamental principles

of acoustic measurement. The tailored Green's function, designed to account for scattering effects in the steering vector, will be introduced in the frequency domain. Following this, the extension of wavelet-based beamforming will be outlined to address scenarios with rotating sources. The usage of tailored Green's function, required in the time-frequency domain, is also specified.

### A. Conventional beamforming for stationary source localization in a scattering environment

The conventional frequency-domain beamforming method is recommended for fast stationary source localization. It typically involves the following sequential steps: recording the sound pressure signal via the microphone array; filtering and converting these signals from the time domain into the frequency domain using the Fourier transform; and steering across various scanning points on the scanning plane to generate the acoustic image, where local areas with high amplitude may indicate sources of sound. The formula for computing an image of sound power  $\mathbf{A}(\omega)$  at the scanning plane utilizing the beamforming algorithm is outlined as follows:

$$\mathbf{A}(\omega) = \mathbf{h}[\mathbf{C}(\omega)\mathbf{h}^*], \quad (1)$$

where the cross-spectral matrix at a specified angular frequency  $\omega$  is expressed as

$$\mathbf{C}(\omega) = \begin{bmatrix} C_{1,1} & C_{1,2} & \cdots & C_{1,N} \\ C_{2,1} & C_{2,2} & \cdots & C_{2,N} \\ \vdots & & \ddots & \vdots \\ C_{N,1} & C_{N,2} & \cdots & C_{N,N} \end{bmatrix}, \quad (2)$$

with  $C_{nn'}(\omega) = \mathbf{Y}_n(\omega)\mathbf{Y}_{n'}^*(\omega)$  and  $n, n' = 1, \dots, N$ . The signal  $\mathbf{Y}_n(\omega)$  represents the outcome of the Fourier transformation at the angular frequency  $\omega$  captured by the  $n$ th microphone, while  $\mathbf{Y}_{n'}^*(\omega)$  denotes the outcome from the  $n'$ th microphone along with an extra conjugate transpose operation superscripted by  $*$ . The diagonal entries of the cross-spectral matrix with  $n = n'$  denote auto-correlation and are generally set to zero to remove self-noise.

$\mathbf{h}$  is a matrix of steering vectors with a size of  $M \times N$ , where  $M$  is the number of scanning points in the scanning plane and  $N$  is the number of microphones. The steering vector plays a crucial role in the beamforming process as it determines the acoustic directivity of the array, representing the amplitude and phase variations for sound propagation between the source and each sensor through Green's function. Typically, the steering vector is classified into four formulations, as outlined by Sarradj (2012), with the fourth formulation being particularly well-suited for accurately obtaining source positions. A variant of the formula from Eq. (5) in Chen *et al.* (2023) is expressed as follows:

$$h_{mn} = \frac{G(\mathbf{x}_m, \mathbf{y}_n; \omega)}{\|\mathbf{G}(\mathbf{x}_m, \mathbf{y}; \omega)\|}, \quad (3)$$

where the symbol  $\|\cdot\|$  denotes  $L_2$ -norm operation,  $G(\mathbf{x}_m, \mathbf{y}_n; \omega)$  is the Green's function from the  $m$ th scanning point at  $\mathbf{x}_m$  to the  $n$ th microphone at  $\mathbf{y}_n$ , and  $\mathbf{G}(\mathbf{x}_m, \mathbf{y}; \omega)$  denotes a vector from  $m$ th scanning point to all microphones.

The free-field Green's function without considering refraction and scattering effects (Amiet, 1978; Ma *et al.*, 2022) is expressed as

$$G_{STD}(\mathbf{x}_m, \mathbf{y}_n; \omega) = \frac{e^{-ikr}}{4\pi r}, \quad (4)$$

where  $r = |\mathbf{x}_m - \mathbf{y}_n|$  denotes the distance between the microphone and the scanning point,  $k$  is the wave number, and  $i$  is the unit complex number.

When acoustically scattering bodies exist, the first option is to separate the scattered pressure from the total sound pressure, retaining only the incident pressure, and process it using a conventional procedure. In an environment where the reverberation path time differences are well separated from the direct propagation path time differences, a filtering operation can be employed to eliminate the reflected waves in the cross-spectral matrix (Fischer and Doolan, 2017). The second option is to include the scattering effects in Green's function and associated beamforming map (Lehmann *et al.*, 2022), which is adopted in this study. To obtain the tailored Green's function numerically, a scattering prediction method is applied to the settings of given scatterers' position, surface impedance, and shape. This scattering prediction method is established with a monopolar equivalent source method and a truncated singular value decomposition method in the frequency domain (Wang *et al.*, 2022; Wang *et al.*, 2020), which is an alternative to the boundary element method. The in-house code for scattering prediction has been well-examined by analytical solutions (Wang *et al.*, 2022). Importantly, the frequency-domain scattering prediction method is also applicable for the subsequent wavelet-based beamforming in the time-frequency domain because the time-frequency method can be regarded as performing frequency-domain beamforming at each moment.

By pre-defining a point source, the total pressure  $p'_{to}(\omega, t)$  at time  $t$ , a combination of incident pressure and scattered pressure, is determined by an inverse Fourier transform and frequency selection of the results from the frequency-domain equivalent source approach.  $p'_{to}(\omega, t)$  is expressed in terms of real and imaginary components, and is then used to obtain the tailored Green's function as

$$G_{ESM}(\mathbf{x}_m, \mathbf{y}_n; \omega) = \frac{p'_{to}(\omega, t)}{e^{i\omega t}}, \quad (5)$$

where  $G_{ESM}(\mathbf{x}_m, \mathbf{y}_n; \omega)$  represents the amplitude decay and phase delay of signals of a specified angular frequency  $\omega$ . Then, the conventional beamforming method, which takes scattering into account, has been established.

## B. Wavelet-based beamforming for rotating source localization in a scattering environment

To consider rotating source localization, Sijtsma *et al.* (2001) extended the delay-and-sum beamforming method to a rotating source identifier shortened as ROSI, where the "de-Dopplerisation" technique is applied in the time domain. Additionally, the deconvolution technique can be combined as outlined in the CLEAN-T method by Cousson *et al.* (2019). In the frequency domain, Dougherty and Walker (2009) proposed a virtual-motion technique to consider the rotating source with a circular phased array. Our recent advancement has led to the development of the wavelet-based beamforming method in the time-frequency domain with consideration of the Doppler effect (Chen and Huang, 2018; Chen *et al.*, 2023; Chen *et al.*, 2020; Chen *et al.*, 2021; Liang *et al.*, 2020). The time-frequency domain method enables the assessment of frequency properties across various snapshots, physically allowing for the dynamic capture of a source that varies in both time and frequency. The Morse wavelet transform originated in 1980 is employed to replace the Fourier transform in the preceding section, facilitating the conversion of time-domain signals into the time-frequency domain. Different from conventional beamforming with a fixed cross-spectral matrix  $\mathbf{C}(\omega)$  at a specific angular frequency  $\omega$ , the cross-spectral matrix  $\mathbf{C}(\omega', t)$  of wavelet-based beamforming further varies with time. The Doppler-shifted angular frequency  $\omega'$  can be obtained from Eq. (24) in Chen and Huang (2018) as

$$\omega' = \omega \cdot \alpha, \quad (6)$$

where  $\alpha$  representing the Doppler effect can be found in Eq. (20) of Chen and Huang (2018) as

$$\alpha = \left( 1 + \frac{\mathbf{v}(t) \cdot (\mathbf{x}_s - \mathbf{y}_a)}{c_0 |\mathbf{y}_a - \mathbf{x}_s|} \right)^{-1}, \quad (7)$$

where  $\mathbf{x}_s$  is the source location and  $\mathbf{y}_a$  is the microphone location.  $\mathbf{v}(t)$  is the rotational velocity and  $c_0$  is the sound speed.

The formula for computing an image of sound power  $\mathbf{A}(\omega, t)$  at the scanning plane is written as follows:

$$\mathbf{A}(\omega, t) = \mathbf{h}[\mathbf{C}(\omega', t)\mathbf{h}^*], \quad (8)$$

where  $C_{nn'}(\omega', t) = \mathbf{Y}_n(\omega', t + \Delta t_n) \mathbf{Y}_{n'}^*(\omega', t + \Delta t_{n'})$  and  $n, n' = 1, \dots, N$ . The microphone signal  $\mathbf{Y}_n(\omega', t + \Delta t_n)$  represents the result of the wavelet transformation at the angular frequency  $\omega'$  and time  $t + \Delta t_n$  captured by the  $n$ th microphone, while  $\mathbf{Y}_{n'}^*(\omega', t + \Delta t_{n'})$  denotes the result from the  $n'$ th microphone along with an extra conjugate transpose operation. The delayed time is written as

$$\Delta t = \Delta \phi / \omega, \quad (9)$$

where  $\Delta \phi$  represents the phase delays obtained from the imaginary part of tailored Green's function.



Regarding the steering vector  $\mathbf{h}$  in Eq. (8), the tailored Green's function for Fourier-based and wavelet-based beamforming methods is identical, as the microphones and scanning points remain stationary. Once the Green's function is determined, it further includes the coefficient of the Doppler effect  $\alpha$  induced by rotation (Chen and Huang, 2018) as follows:

$$G'_{ESM}(\mathbf{x}_m, \mathbf{y}_n; \omega) = G_{ESM}(\mathbf{x}_m, \mathbf{y}_n; \omega) \alpha^2. \quad (10)$$

Therefore, the tailored Green's function is applicable to both stationary and rotational sources, with the latter requiring consideration of the Doppler coefficient as outlined in Eq. (10). When the rotational speed is low and the Doppler effect is negligible, the steering vectors of both Fourier-based and wavelet-based beamforming methods are identical. In such cases, the primary distinction between these two methods lies in the cross-spectral matrix, which is constructed from the microphone signals following Fourier or wavelet transformation. The selection of transformed microphone signals in the wavelet transform necessitates knowledge of the delayed time related to source motion and body scattering, thereby governing the dynamic capture of sources that vary in both time and frequency. After selecting the transformed signals, the acoustic imaging process of wavelet-based beamforming is the same as that of Fourier-based beamforming. If the source is stationary, it is reasonable to conclude that wavelet-based beamforming closely resembles conventional frequency-domain beamforming; however, it is essential to incorporate the time delay in wavelet-based beamforming to achieve results consistent with those obtained through conventional methods. In environments with scattering bodies, the time delay in Eq. (9) is further influenced by the scattering effect, which must be considered through the tailored Green's function.

From the above discussion, it is apparent that the tailored Green's function is a key factor for beamforming within a complex scattering environment. This tailored Green's function determines the time-domain parameter known as delayed time and the frequency-domain parameter referred to as the steering vector. The delayed time and selected frequency further determine the cross-spectral matrix in the time-frequency domain. To efficiently obtain the tailored Green's function, the reciprocity of sound propagation is used in that the propagation from the scanning points in the source plane to the microphone array can be reversely replaced by the propagation from the microphone array to the scanning points in the source plane. This principle is suitable for multipoles including monopoles, dipoles, and quadrupoles (Chambon *et al.*, 2022). In cases of reciprocal propagation, the tailored Green's function at a specific frequency can be computed with a limited number of calculations equal to the total number of microphones in the array. The increased computational time compared to theoretical free-field Green's function is dependent on the specific case at hand. Certainly, the primary advantage of tailored Green's functions is their ability to capture both

exterior and interior propagation characteristics in the presence of scatterers, making them potentially applicable to various scenarios, including cabin, duct, and fuselage cases.

### III. RESULTS AND DISCUSSIONS

Throughout this section, both the stationary and rotational source localization will be examined in three scenarios: beamforming using free-field Green's function in the absence of a scatterer; beamforming using free-field Green's function in the presence of a scatterer; and beamforming using tailored Green's function in the presence of a scatterer. A spherical scatterer of diameter 0.3 m and a 56-microphone array of diameter 0.7 m are selected.

#### A. Stationary source localization in the presence of a scattering body

In this subsection, cases of spherical scattering are employed to examine the performance of tailored Green's function in localizing stationary sound sources. An analytical solution is utilized to model the pressure signals originating from the sound source, scattered by a sphere, and subsequently captured by the spiral microphone array (Siozos-Rousoulis *et al.*, 2017). As depicted in Fig. 1, a sound source with unit amplitude, a frequency of 6 kHz, and at three different positions of (0.0, 0.0, 0.5) m, (0.1, 0.0, 0.5) m, and (0.2, 0.0, 0.5) m is selected for analysis. The scatterer is centered at (0, 0, 0) m, and the microphone array is positioned at (0, 0, -1) m along the  $x$ - $y$  plane.

Figure 2 illustrates the source strength defined by  $\Delta$ SPL of conventional beamforming utilizing both the free-field Green's and tailored Green's functions in the presence or absence of a scatterer.  $\Delta$ SPL denotes the difference obtained by subtracting the maximum SPL, where the SPL is calculated with  $10 \log_{10}(A/p_{\text{ref}}^2)$  and  $p_{\text{ref}} = 2 \times 10^{-5}$  Pa. A grid of  $50 \times 50$  scanning points is used in the scanning plane. As can be expected in Figs. 2(a)–2(c), the application of free-field Green's function in free space yields ideal results across different sound source locations. However, in the

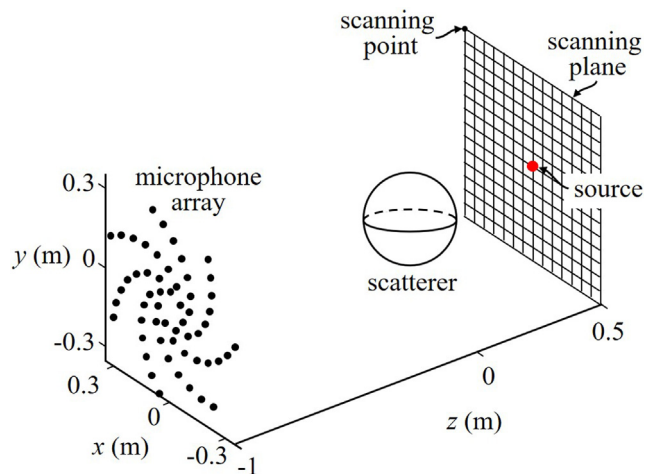


FIG. 1. (Color online) Sketch of beamforming for a sound source behind a scatterer.

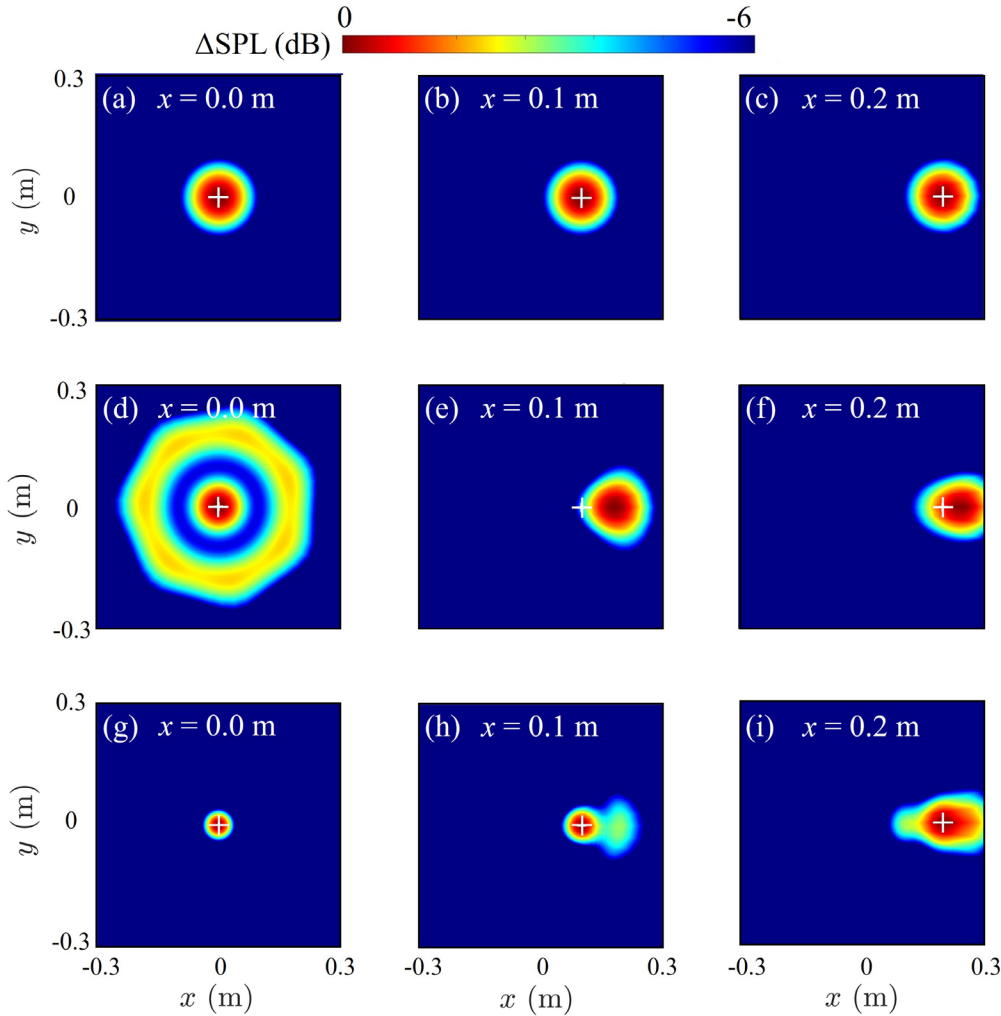


FIG. 2. (Color online) Conventional beamforming results of one sound source using (a)–(c) the free-field Green’s function in the absence of a scatterer, (d)–(f) the free-field Green’s function in the presence of a scatterer, and (g)–(i) the tailored Green’s function in the presence of a scatterer, respectively. The positions of the source range from  $x = 0.0$  m to  $0.2$  m. The white plus signs indicate the actual source location.

presence of a scatterer, the characteristics of sound wave propagation deviate from those observed in free field conditions. At this time, the magnitude of the scattered wave approaches or even exceeds that of the incident wave. If the original Green’s function continues to be used, the resulting acoustic images will reasonably change. In Fig. 2(d), a special case is presented wherein the sound source can still be localized when the sound source is shielded by the scatterer due to the rotational symmetry of both the sphere and the array. Meanwhile, the mainlobe, representing the sound source region, is surrounded by a strong annular sidelobe. When shifting the sound source away from the central axis, localization errors occur with the usage of the free-field Green’s function, as shown in Figs. 2(e) and 2(f). The localization error associated with the former is more pronounced than that of the latter.

Beyond the aforementioned, the tailored Green’s function is computed using 2680 grid points and equivalent sources through the equivalent source method, with the top 1500 eigenvalues retained during the singular value decomposition process. The position of the equivalent source surface is a scaled replica of the scattering surface with a ratio of 0.85.

The CPU time for 56 computations of tailored Green’s function in a workstation equipped with 128 GB of random access memory and an AMD Ryzen 5965WX CPU (AMD, Santa Clara, CA) is about 4 min per frequency. Once computed, tailored Green’s functions can be stored and utilized for sound sources across various positions and motions on the scanning plane. Upon introducing the tailored Green’s function, it can be found that the localized sound source position is close to the actual source position in Figs. 2(g)–2(i). This means that the tailored Green’s function can enhance the accuracy of beamforming results in the current shielding or scattering environment. The presence of side lobes is also a characteristic feature of this type of Green’s function. Upon comparing Figs. 2(g)–2(i) with Figs. 2(a)–2(c), an interesting observation emerges, indicating that the sound source is confined within a relatively smaller region, thereby suggesting an improvement in spatial resolution. Meanwhile, the difference between Figs. 2(g)–2(i) with resolution improvement and Figs. 2(e) and 2(f) without resolution improvement lies in the steering vector. The improved resolution may be caused by the changes in phase

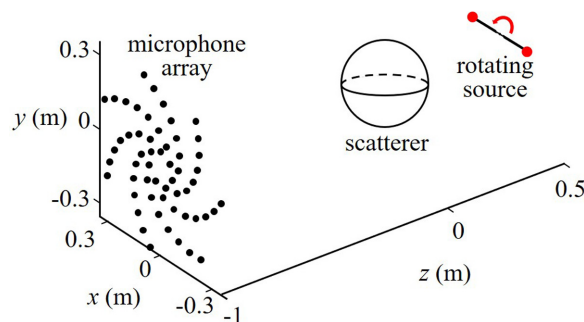


FIG. 3. (Color online) Sketch of rotating sound sources behind a scatterer.

and amplitude in tailored Green's function, which can be viewed as a virtual manipulation of the position and weighting of the physical microphones in the beamforming process. Another interpretation of electromagnetism is that the tailored Green's function incorporates additional reflections, diffractions, and shadowing effects, in a way that adds more virtual microphones to the microphone array (Henty and Stancil, 2004).

In summary, this subsection explores the efficacy of coupling tailored Green's functions with conventional beamforming, providing preliminary validation of its performance in the localization of stationary sources.

## B. Rotating source localization in the presence of a scattering body

In this subsection, the performance of wavelet-based beamforming with tailored Green's function in localizing rotating sound sources is numerically examined. Figure 3 shows a sketch of two sound sources rotating around  $z$  coordinate and behind a scatterer, which serves as a simplistic representation of rotor vehicles in general. The coordinate origin is set at the center of the scatterer, where the microphone array is centered at  $(0, 0, -1)$  m. The monopole sound sources are located in the scanning plane  $z = 0.5$  m with a spacing of  $0.2$  m and a rotating frequency of  $5$  revolutions per second in a quasi-stationary manner. The rotational center axis of the sound source, the scatterer's center, and the microphone's center axis are coaxial, ensuring

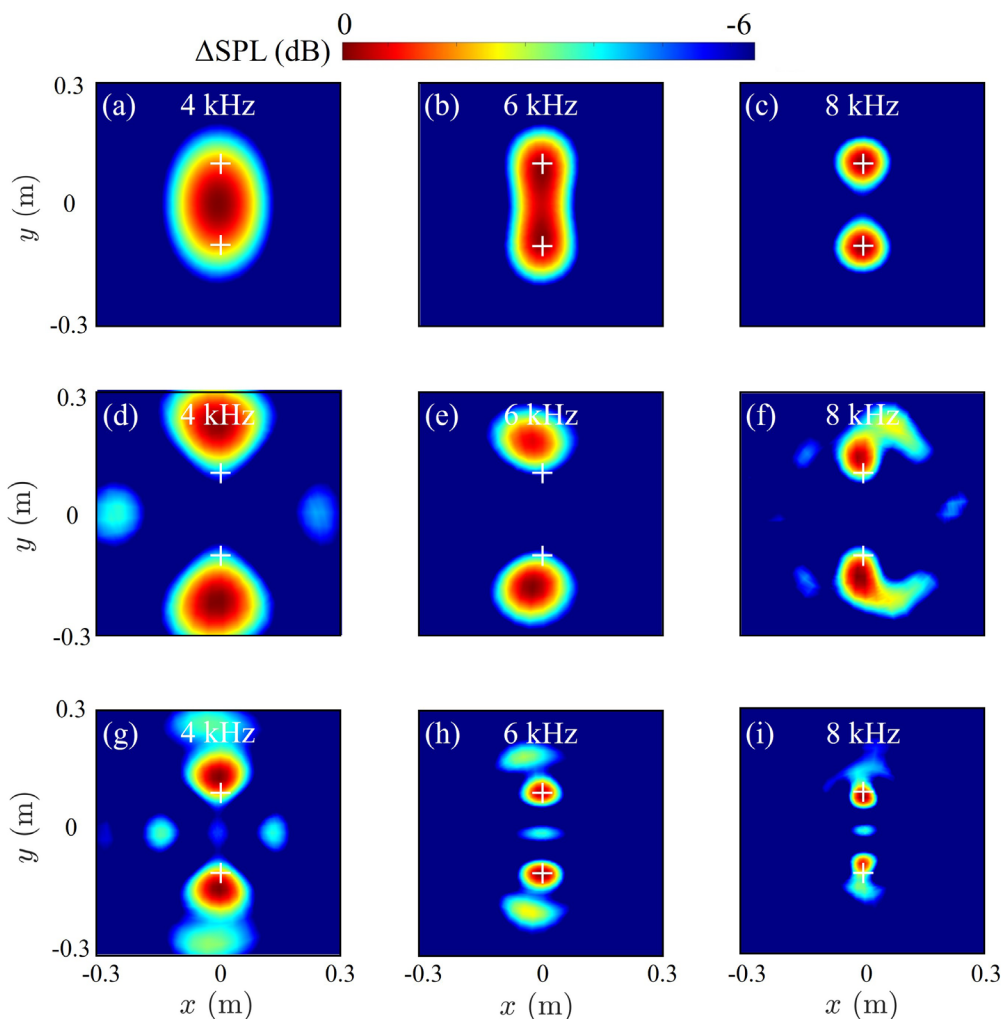


FIG. 4. (Color online) Numerical beamforming results of rotating sound sources using (a)–(c) the free-field Green's function in the absence of a scatterer, (d)–(f) the free-field Green's function in the presence of a scatterer, and (g)–(i) the tailored Green's function in the presence of a scatterer, respectively. The white plus signs indicate the actual source locations.

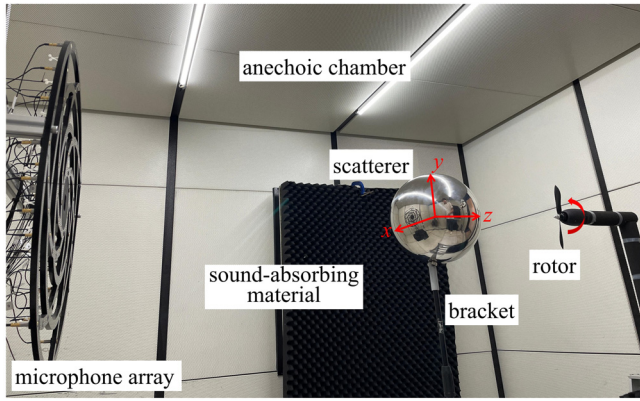


FIG. 5. (Color online) Experimental setup of beamforming with scattering.

consistency in the imaging results at each instant. In this scenario, the instantaneous acoustic image in which the sound sources rotate into the  $y$  coordinate is selected for visualization subsequently.

Using the rotating monopoles, the time-domain pressure gradient on the surface of the scatterer can be obtained,

which is then transformed into the frequency domain to serve as a boundary condition for the equivalent source method. The corresponding scattered sound pressure at different microphones is numerically computed, superimposed with incident sound pressure, and finally converted back into the time domain to function as input for wavelet-based beamforming. Figure 4 illustrates the acoustic images in three scenarios at varying frequencies. As seen in Fig. 4(a), the sources of frequency  $f = 4$  kHz are not resolved well by wavelet-based beamforming due to the limitation of the resolution according to the Rayleigh criterion (Chen *et al.*, 2022), and the source region is mixed in one connected domain. As the frequency increases to 6 and 8 kHz, the two sources are gradually resolved, and the source positions are close to the white plus signs in Figs. 4(b) and 4(c), indicating that the sound sources are accurately identified. Different from the beamforming results in an ideal free-space environment, the complexity of introducing a scatterer increases. If the free-field Green's function continues to be used, the localized sound sources will show large deviations as seen in Figs. 4(d)–4(f). The localized source positions

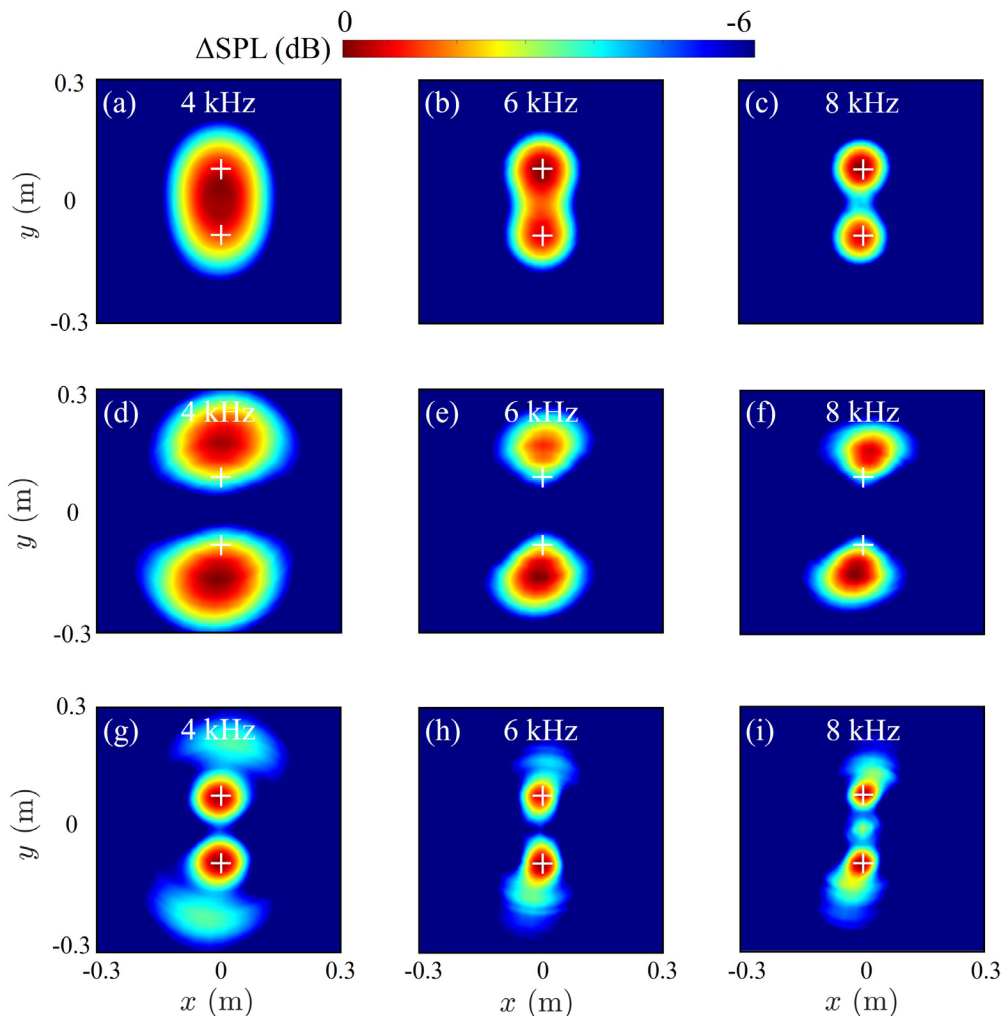


FIG. 6. (Color online) Experimental beamforming results with the scatterer positioned at (0.0, 0.0, 0.0) m: (a)–(c) the free-field Green's function in the absence of a scatterer, (d)–(f) the free-field Green's function in the presence of a scatterer, and (g)–(i) the tailored Green's function in the presence of a scatterer. The white plus signs indicate the actual source locations.



shift outward from the actual positions, which is consistent with the observations in Figs. 2(e) and 2(f). With consideration of the tailored Green's function, the accuracy of source position can be comparably improved as shown in Figs. 4(g)–4(i). It is also evident that the resolution in a scattering environment is higher than that in a free space. For example, the two sound sources are resolved by wavelet-based beamforming in Fig. 4(g) instead of in Fig. 4(a).

Therefore, the efficacy of coupling tailored Green's functions with wavelet-based beamforming is validated for the localization of rotating sources. Subsequently, experiments will be conducted to further examine these findings.

### C. Experimental examination of rotating source localization

Before detailing the experimental setup, it is important to note the similarities and differences between experimental and computational conditions. On one hand, the experiments utilize the same tailored Green's function as employed in the numerical cases. Conversely, the sound source in the experiment is characterized as Gaussian, broadband, and particularly unsteady, with the intensity of the rotor sound source fluctuating instantly. Thus, all experimental results are averaged within a rotating coordinate system to exclude the intermittent characteristics.

As shown in Fig. 5, the acoustic experiments were conducted in a  $3.2\text{ m} \times 3.1\text{ m} \times 2.0\text{ m}$  anechoic chamber (Yi *et al.*, 2021). The chamber is engineered with a cut-off frequency of 200 Hz, and both the wind tunnel nozzles and collection ports are lined with porous materials to minimize sound reflection. During the experiments, a two-blade rotor,

referred to as SP2 (Jiang *et al.*, 2022) and developed by our group, was employed to generate rotating sound sources with a passing frequency of 120 revolutions per second. The emitted sound waves, exhibiting broadband and transient characteristics, were scattered by a stationary scatterer in no-flow conditions and captured by a 56-microphone array. The rotor features a diameter of 0.23 m, and the microphone array corresponds to the previously discussed numerical example. A stainless steel sphere, measuring 300 mm in diameter served as a rigid scatterer.

Consistent with the numerical condition, the distance between the plane of rotor rotation and the center of the scatterer is first set at 0.5 m, whereas the distance between the centers of the microphone array and scatterer is 1 m. Figure 6 shows the experimental acoustic images obtained with wavelet-based beamforming within a rotating coordinate system. The acoustic imaging results in the free-space cases include the bracket but without the scatterer. At a frequency of 4 kHz, the sound sources are identified as one region, as shown in Fig. 6(a); at higher frequencies, the two sound sources can be better distinguished, as shown in Figs. 6(b) and 6(c). When a scatterer is installed between the microphone array and the sound source, if the free-field Green's function is still used in the steering vector, it can be found that the localized sound source position deviates from the white plus signs, as shown in Figs. 6(d)–6(f). If a tailored Green's function is used in the steering vector, it can be found that the localized sound source position is relatively close to the white plus signs. By comparing Figs. 6(a)–6(c) with Figs. 6(g)–6(i), it can also be seen that the resolution of sound sources is improved after introducing scattering. In other words, the

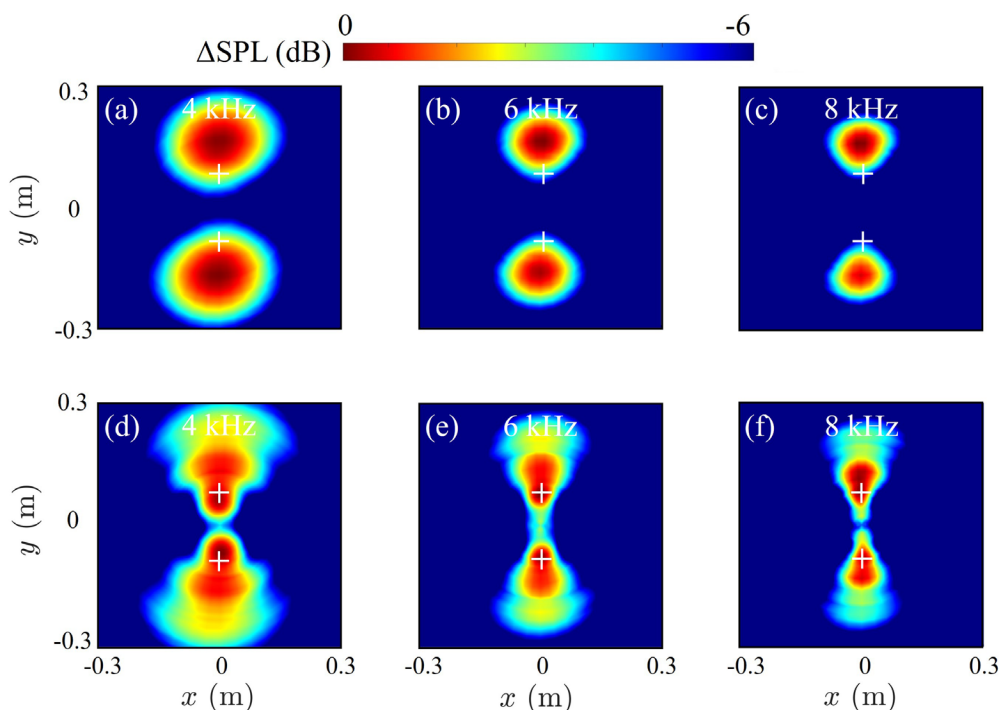


FIG. 7. (Color online) Experimental beamforming results with the scatterer positioned at (0.0, 0.0, 0.2) m: (a)–(c) the free-field Green's function and (d)–(f) the tailored Green's function in the presence of a scatterer. The white plus signs indicate the actual source locations.

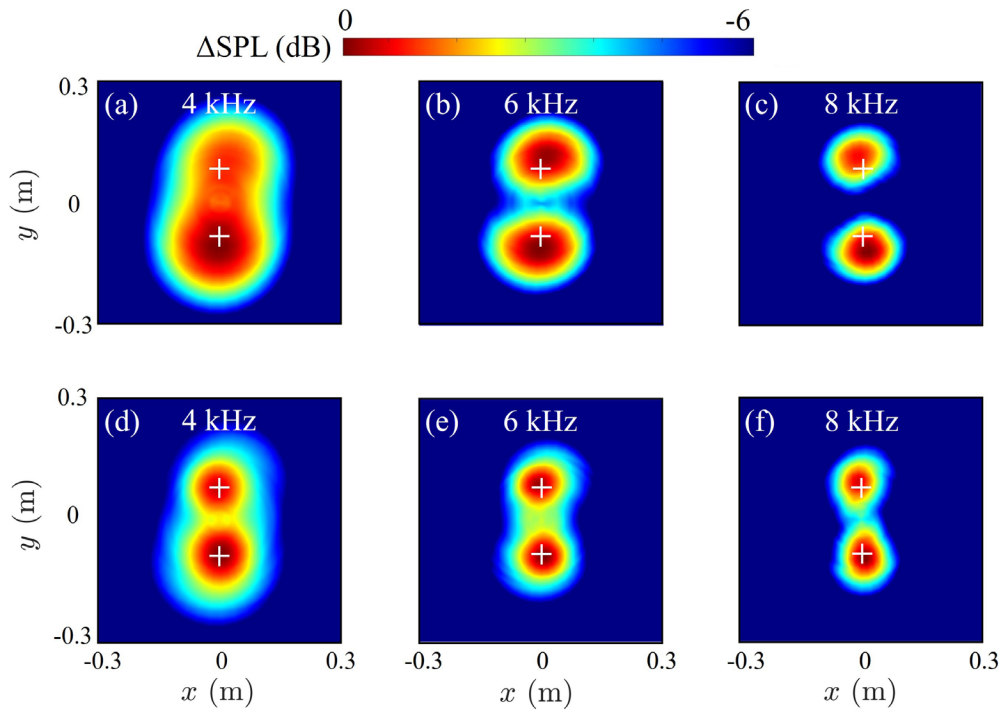


FIG. 8. (Color online) Experimental beamforming results with the scatterer positioned at (0.0, 0.1, 0.0) m: (a)–(c) the free-field Green's function and (d)–(f) the tailored Green's function in the presence of a scatterer. The white plus signs indicate the actual source locations.

resolution improvement phenomenon also exists in the experimental rotating configurations. By counting the positions of the maximum SPL values in each frame of the acoustic image, the average radius of the rotation path in free space is determined to be 0.079 m for both frequencies of 6 and 8 kHz, respectively. In the presence of a scatterer and employing the free-field Green's function, the averaged radius at frequencies of 4, 6, and 8 kHz measures 0.171, 0.165, and 0.159 m, respectively. When utilizing the tailored Green's function, the averaged radius is adjusted to 0.088, 0.084, and 0.086 m, respectively. It is evident that the tailored Green's function yields results significantly closer to those observed in free space, whereas the free-field Green's function demonstrates larger discrepancies.

Keeping the position of the microphone array and rotor constant, the center of the scatterer is repositioned to (0.0, 0.0, 0.2) m and (0.0, 0.1, 0.0) m. The corresponding acoustic images are presented in Figs. 7 and 8, respectively. It is evident that when the scatterer is closer to the rotor, its shielding effect on the sound waves emitted by the rotor becomes more pronounced. At this point, the sound source positions are obtained using the free-field Green's function, as shown in Figs. 7(a)–7(c), are consistently offset radially outward, whereas the tailored Green's function yields more accurate results. Additionally, when the scatterer is not collinear with the array center and the rotation center, the results that are based on tailored Green's function in Figs. 8(d)–8(f) continue to provide relatively acceptable results. Therefore, the methodology of combining tailored Green's function with wavelet-based beamforming is confirmed to be effective in the present cases.

#### IV. CONCLUSIONS

In this study, tailored Green's functions, along with the corresponding delayed time, are calculated numerically through an equivalent source approach, which is then integrated into the conventional and wavelet-based beamforming methods. These techniques have been verified through numerical simulations and experimental measurements involving spherical scattering. The application of tailored Green's functions in scattering scenarios can enhance the resolution of acoustic imaging, particularly at a frequency of 4 kHz, compared to situations employing free-field Green's functions in free-field environments. Furthermore, across various frequencies and sphere positions and within a shielded environment, the results obtained from tailored Green's functions are confirmed to be more accurate than those obtained from free-field Green's functions. Future research could investigate the application of artificial intelligence methods to accelerate the computation of tailored Green's functions, given their case-dependent nature.

#### ACKNOWLEDGMENTS

This work is conducted at the AVIC-HKUST Aeroacoustics United Technology Centre, and it is partially supported by the Hong Kong Research Grants Council No. 16202519, and the National Natural Science Foundation of China Grants Nos. 12302345 and 12402314.

#### AUTHOR DECLARATIONS

##### Conflict of Interest

The authors have no conflict of interest to disclose.

## DATA AVAILABILITY

The data that support the findings of this study are available within the article.

- Amiet, R. (1978). "Refraction of sound by a shear layer," *J. Sound Vib.* **58**(4), 467–482.
- Amiet, R. K. (1975). "Acoustic radiation from an airfoil in a turbulent stream," *J. Sound Vib.* **41**(4), 407–420.
- Bahr, C. J., Zawodny, N. S., Bertolucci, B., Li, J., Sheplak, M., and Cattafesta, L. N. (2015). "A plasma-based non-intrusive point source for acoustic beamforming applications," *J. Sound Vib.* **344**, 59–80.
- Bousabaa, S., Bulté, J., Mincu, D.-C., Marchiano, R., and Ollivier, F. (2018). "Sparse Green's functions estimation using orthogonal matching pursuit: Application to aeroacoustic beamforming," *AIAA J.* **56**(6), 2252–2270.
- Brooks, T. F., and Humphreys, W. M. (2006). "A deconvolution approach for the mapping of acoustic sources (DAMAS) determined from phased microphone arrays," *J. Sound Vib.* **294**(4–5), 856–879.
- Chambon, J., Antoni, J., and Bouley, S. (2022). "Galerkin equivalent sources method for sound field reconstruction around diffracting bodies," *J. Acoust. Soc. Am.* **152**(4), 2042–2053.
- Chen, W., and Huang, X. (2018). "Wavelet-based beamforming for high-speed rotating acoustic source," *IEEE Access* **6**, 10231–10239.
- Chen, W., Jiang, H., and Huang, X. (2022). "Super-resolution acoustic imaging," *Appl. Phys. Lett.* **120**(11), 112201.
- Chen, W., Ma, Z., Étienne, S., Guo, J., Zhou, P., Zhong, S., Zhang, X., and Huang, X. (2023). "Acoustic imaging of the broadband noise arising in contra-rotating co-axial propellers," *Aerosp. Sci. Technol.* **141**, 108531.
- Chen, W., Peng, B., Liem, R. P., and Huang, X. (2020). "Experimental study of airfoil-rotor interaction noise by wavelet beamforming," *J. Acoust. Soc. Am.* **147**(5), 3248–3259.
- Chen, W., Yang, Z., Peng, B., and Huang, X. (2021). "On trailing edge noise from propellers with interactions to shear layers," *J. Sound Vib.* **495**, 115901.
- Chiariotti, P., Martarelli, M., and Castellini, P. (2019). "Acoustic beamforming for noise source localization—reviews, methodology and applications," *Mech. Syst. Sig. Process.* **120**, 422–448.
- Cousson, R., Leclère, Q., Pallas, M.-A., and Bérengier, M. (2019). "A time domain CLEAN approach for the identification of acoustic moving sources," *J. Sound Vib.* **443**, 47–62.
- Dougherty, R., and Walker, B. (2009). "Virtual rotating microphone imaging of broadband fan noise," in *Proceedings of the 15th AIAA/CEAS Aeroacoustics Conference*, May 11–13, Miami, FL, pp. 2009–3121.
- Dougherty, R. P. (2014). "Functional beamforming," in *Proceedings of the 5th Berlin Beamforming Conference*, June 10–11, Berlin, Germany, pp. 1–25.
- Fenech, B., and Takeda, K. (2007). "Towards more accurate beamforming levels in closed-section wind tunnels via de-reverberation," in *Proceedings of the 13th AIAA/CEAS Aeroacoustics Conference*, May 21–23, Rome, Italy, pp. 2007–3431.
- Fischer, J., and Doolan, C. (2017). "Improving acoustic beamforming maps in a reverberant environment by modifying the cross-correlation matrix," *J. Sound Vib.* **411**, 129–147.
- Guidati, S., Brauer, C., and Wagner, S. (2002). "The reflection canceller-phased array measurements in a reverberating environment," in *Proceedings of the 8th AIAA/CEAS Aeroacoustics Conference & Exhibit*, June 17–19, Breckenridge, CO, pp. 2002–2462.
- Guo, Y. (2024). "Phased microphone array on aircraft fuselage," in *Proceedings of the 30th AIAA/CEAS Aeroacoustics Conference*, June 4–7, Rome, Italy, pp. 2024–3010.
- Henty, B. E., and Stancil, D. D. (2004). "Multipath-enabled super-resolution for rf and microwave communication using phase-conjugate arrays," *Phys. Rev. Lett.* **93**(24), 243904.
- Hirayama, R., Christopoulos, G., Martínez Plasencia, D., and Subramanian, S. (2022). "High-speed acoustic holography with arbitrary scattering objects," *Sci. Adv.* **8**(24), eabn7614.
- Huang, X., Bai, L., Vinogradov, I., and Peers, E. (2012). "Adaptive beamforming for array signal processing in aeroacoustic measurements," *J. Acoust. Soc. Am.* **131**(3), 2152–2161.
- Jiang, H., Wu, H., Chen, W., Zhou, P., Zhong, S., Zhang, X., Zhou, G., and Chen, B. (2022). "Toward high-efficiency low-noise propellers: A numerical and experimental study," *Phys. Fluids* **34**(7), 076116.
- Lacombe, R., Föller, S., Jasor, G., Polifke, W., Aurégan, Y., and Moussou, P. (2013). "Identification of aero-acoustic scattering matrices from large eddy simulation: Application to whistling orifices in duct," *J. Sound Vib.* **332**(20), 5059–5067.
- Lehmann, M., Ernst, D., Schneider, M., Spehr, C., and Lummer, M. (2022). "Beamforming for measurements under disturbed propagation conditions using numerically calculated Green's functions," *J. Sound Vib.* **520**, 116638.
- Lehmann, M., Ernst, D., Spehr, C., Schneider, M., and Lummer, M. (2024). "Rotating beamforming method for the use of tailored Green's functions," in *Proceedings of the 10th Berlin Beamforming Conference*, June 10–11, Berlin, Germany, pp. 1–18.
- Liang, S., Chen, W., Liem, R. P., and Huang, X. (2020). "Experimental analysis of cooling fan noise by wavelet-based beamforming and proper orthogonal decomposition," *IEEE Access* **8**, 121197–121203.
- Ma, R., Zhang, S., Luo, Y., Han, S., Wang, Y., and Wang, X. (2022). "Numerical study on multiple acoustic scattering by a vortex array," *J. Sound Vib.* **527**, 116815.
- Mao, Y., Cai, J., Gu, Y., and Qi, D. (2015). "Direct evaluation of acoustic-intensity vector field around an impedance scattering body," *AIAA J.* **53**(5), 1362–1371.
- Merino-Martínez, R., Sijtsma, P., Snellen, M., Ahlefeldt, T., Antoni, J., Bahr, C. J., Blacodon, D., Ernst, D., Finez, A., Funke, S., Geyer, T. F., Haxter, S., Herold, G., Huang, X., Humphreys, W. M., Leclerc, Q., Malgozar, A., Michel, U., Padois, T., Pereira, A., Picard, C., Sarrahd, E., Siller, H., Simons, D. G., and Sephr, C. (2019). "A review of acoustic imaging methods using phased microphone arrays: Part of the 'aircraft noise generation and assessment' special issue," *CEAS Aeronaut. J.* **10**, 197–230.
- Sagaga, J., and Lee, S. (2024). "High-fidelity computational study of aerodynamic noise of side-by-side rotor in full configuration," *J. Sound Vib.* **592**, 118607.
- Sarradj, E. (2012). "Three-dimensional acoustic source mapping with different beamforming steering vector formulations," *Adv. Acoust. Vib.* **2012**(1), 292695.
- Sarradj, E. (2017). "A fast ray casting method for sound refraction at shear layers," *Int. J. Aeroacoustics* **16**(1–2), 65–77.
- Sijtsma, P. (2007). "CLEAN based on spatial source coherence," *Int. J. Aeroacoust.* **6**(4), 357–374.
- Sijtsma, P., Oerlemans, S., and Holthusen, H. (2001). "Location of rotating sources by phased array measurements," in *Proceedings of the 7th AIAA/CEAS Aeroacoustics Conference and Exhibit*, May 28–30, Maastricht, the Netherlands, pp. 2001–2167.
- Siozos-Rousoulis, L., De Troyer, T., and Ghorbaniasl, G. (2017). "Scattered noise prediction using acoustic velocity formulations V1A and KV1A," *Wave Motion* **72**, 363–376.
- Vieira, A., Snellen, M., Malgozar, A. M. N., Merino-Martínez, R., and Simons, D. G. (2019). "Analysis of shielding of propeller noise using beamforming and predictions," *J. Acoust. Soc. Am.* **146**(2), 1085–1098.
- Wang, L., Chen, R., You, Y., Wang, Z., and Song, Q. (2022). "An efficient frequency-domain prediction method for aeroacoustic radiation and scattering using equivalent sources," *J. Sound Vib.* **534**, 117039.
- Wang, Z., Rienstra, S. W., Bi, C., and Koren, B. (2020). "An accurate and efficient computational method for time-domain aeroacoustic scattering," *J. Comput. Phys.* **412**, 109442.
- Yi, W., Zhou, P., Fang, Y., Guo, J., Zhong, S., Zhang, X., Huang, X., Zhou, G., and Chen, B. (2021). "Design and characterization of a multifunctional low-speed anechoic wind tunnel at HKUST," *Aerosp. Sci. Technol.* **115**, 106814.
- Zhong, S., Wei, Q., and Huang, X. (2013). "Compressive sensing beamforming based on covariance for acoustic imaging with noisy measurements," *J. Acoust. Soc. Am.* **134**(5), EL445–EL451.
- Zhong, S., Zhang, X., Peng, B., and Huang, X. (2020). "An analytical correction to Amiet's solution of airfoil leading-edge noise in non-uniform mean flows," *J. Fluid Mech.* **882**, A29.
- Zhou, Y., Diaz, M. A., Marx, D., Marchiano, R., Prax, C., and Valeau, V. (2024). "Localizing aeroacoustic sources in complex geometries: A hybrid method coupling 3D microphone array and time-reversal," *J. Sound Vib.* **584**, 118452.